ADVANCED MATERIALS

Supporting Information

for *Adv. Mater.*, DOI 10.1002/adma.202500556

Observation of Nonlinear Topological Corner States Originating from Different Spectral Charges

Victor O. Kompanets, Suge Feng, Yiqi Zhang, Yaroslav V. Kartashov*, Yongdong Li, Sergei A. Zhuravitskii, Nikolay N. Skryabin, Alexander V. Kireev, Ivan V. Dyakonov, Alexander A. Kalinkin, Ce Shang, Sergei P. Kulik, Sergey V. Chekalin and Victor N. Zadkov*

Supporting Information *of* Observation of nonlinear topological corner states originating from different spectral charges

Victor O. Kompanets[1,†], *Suge Feng*[2,†], *Yiqi Zhang*[2,†,*], *Yaroslav V. Kartashov*[1,*], *Yongdong Li*[2], *Sergei A. Zhuravitskii*[1,3], *Nikolay N. Skryabin*[1,3], *Alexander V. Kireev*[1], *Ivan V. Dyakonov*[3], *Alexander A. Kalinkin*[1,3], *Ce Shang*[4], *Sergei P. Kulik*[3], *Sergey V. Chekalin*[1], *Victor N. Zadkov*[1,4]

[1] Institute of Spectroscopy, Russian Academy of Sciences, Troitsk, Moscow 108840, Russia
[2] Key Laboratory for Physical Electronics and Devices, Ministry of Education, School of Electronic Science and Engineering, Xi'an Jiaotong University, Xi'an 710049, China
[3] Quantum Technology Centre, Faculty of Physics, M. V. Lomonosov Moscow State University, Moscow 119991, Russia
[4] Aerospace Information Research Institute, Chinese Academy of Sciences, Beijing 100094, China
[5] Faculty of Physics, Higher School of Economics, Moscow 105066, Russia
[†] These authors contributed equally to this work.
[*] Email Address: zhangyiqi@xjtu.edu.cn, kartashov@isan.troitsk.ru

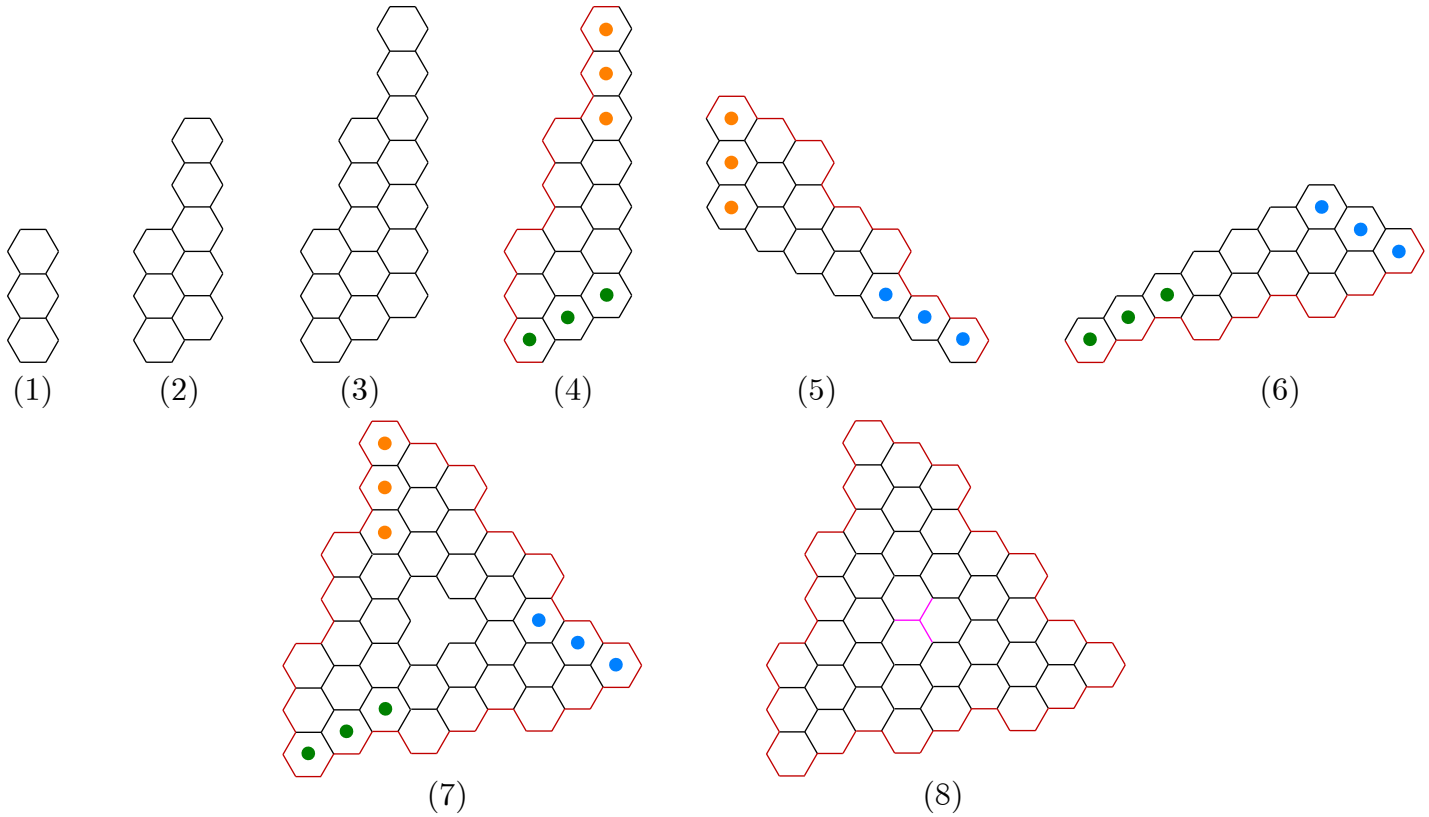

Figure S1: **Construction procedure of the higher-order topological insulators from the main text**. The colored dots in (4) ∼ (6) indicate which unit cells should be emerged.

1 Construction procedure of the higher-order topological insulator with multiple corners

By taking the $\mathcal{H}_3$ structure as an example, the procedure of construction of array with hybrid edges is illustrated in Fig. S1.

(1) First of all, we stack n unit cells vertically. The size of the constructed higher-order topological insulator (HOTI) is determined by the number of n. Since we take the $\mathcal{H}_3$ HOTI as an example, here $n = 3$.

(2) Stack $n + (n-1) = 2n - 1$ unit cells vertically, shift them upward by half of the unit cell, and combine them with the stacked unit cells in (1).

(3) Repeat the operation in (2) to vertically stack $(2n-1) + (n-1) = 3n - 2$ unit cells. Now, $6n - 3$ unit cells have been stacked.

(4) Highlight the left boundary of the stacked unit cells in (3).

(5) Rotate the structure in (4) clockwise by $2\pi/3$.

(6) Rotate the structure in (5) clockwise by $2\pi/3$.

(7) Combine the three structures in (4), (5), and (6) by overlapping the unit cells with same color dots to form a structure with the $\mathcal{C}_3$ discrete rotational symmetry. The red boundaries of the structures in (4), (5), and (6) form a whole boundary with multiple corners.

(8) Fill the missed unit cells with magenta lines. The HOTI with multiple corners and hybrid edges has been constructed.

2 Spectrum of HOTIs with different size

We show the linear spectra of HOTIs with different size in Fig. S2. Clearly, one finds that the spectra of the $\mathcal{H}_2$ [Fig. S2(a)] and $\mathcal{H}_4$ [Fig. S2(b)] configurations are qualitatively similar to spectrum of the $\mathcal{H}_3$ array presented in Fig. 2(a) in the main text.

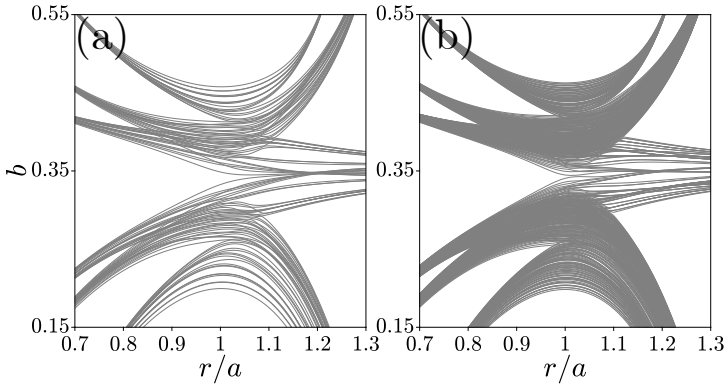

Figure S2: **Comparison of spectra of lattices of different size.** (a) Spectrum of the $\mathcal{H}_2$ lattice. (b) Spectrum of the $\mathcal{H}_4$ lattice. The parameters of individual waveguides are the same as in Fig. 2(a) from main text.

3 Linear stability analysis results

By solving Eq. (5) in the **Methods** section in the main text, we show the dependence $\max\{\beta_{\mathrm{re}}(b)\}$ corresponding to the three nonlinear corner state families in Fig. S3. For the nonlinear state families in Figs. 3(a) and 3(b) in the main text, the perturbation growth rate becomes nonzero only when the nonlinear corner states enter into the bulk band (indicated with gray color) and hybridize with bulk states, as shown in Figs. S3(a) and S3(b). In the band gap, the nonlinear corner states are stable. However nonlinear state bifurcating from the linear corner state numbered 91 in Fig. 3(c) in the main text becomes unstable from $b \sim 0.43$ which is still in the topological gap.

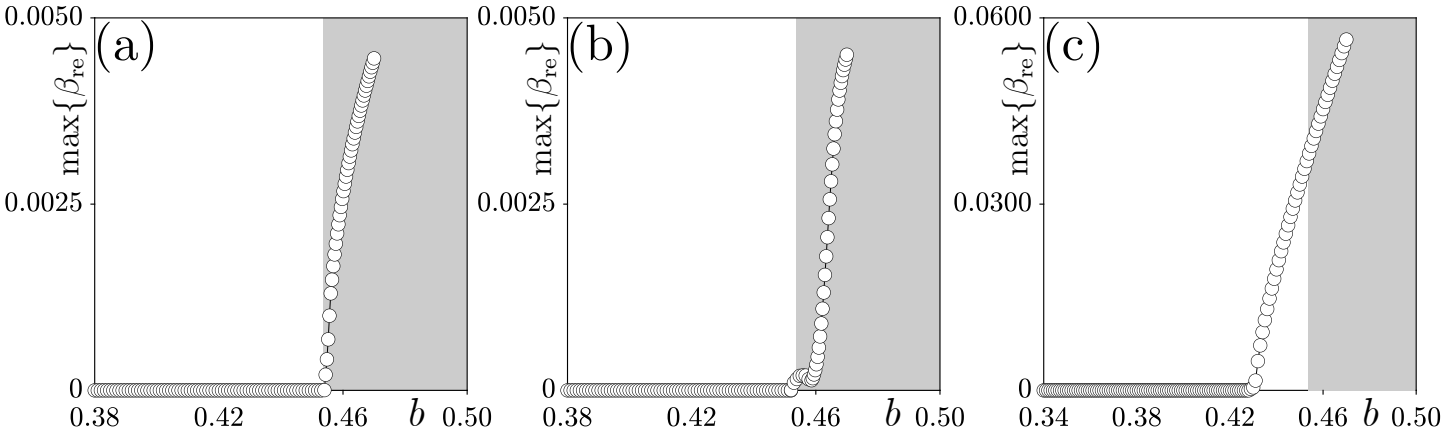

Figure S3: **Stability analysis of nonlinear corner states.** Maximal real part of the perturbation growth rate $\beta_{\rm re}$ versus propagation constant b for the nonlinear corner state families in Fig. 3 in the main text.

4 Other configurations

4.1 The $\mathcal{C}_6$ configuration with hybrid edges

As stated in the main text, corner states arising due to fractional spectral charges can arise not only in $\mathcal{C}_3$-symmetric configuration. Here we provide another configuration with $\mathcal{C}_6$ discrete rotational symmetry that also supports corner states with various fractional charges. This configuration is depicted in Figs. S4(d) and S4(e). One can see that it also has hybrid boundary involving zigzag and armchair segments. As before, the shift of the waveguides within the unit cells is controlled by shift parameter r, as schematically illustrated in Fig. 1 in the main text. Linear spectrum of this configuration as a function of shift parameter r is displayed in Fig. S4(a) and it is qualitatively similar to linear spectrum of the $\mathcal{C}_3$-symmetric structure presented in Fig. 2(a) in the main text. The analysis of the spectral charges based on the locations of the Wannier centers is presented in Fig. S4(d) for trivial phase at $r/a = 0.8$ (Wannier centers are in the middle of the unit cells), and in Fig. S4(e) for crystalline topological phase at $r/a = 1.2$ (Wannier centers shift to the borders between unit cells). In the latter case, there are multiple unit cells with fractional spectral charge 5/6 located close to each other and on this reason corresponding corner states with indices $139 \sim 159$ and close eigenvalues in Fig. S4(c) can hardly be isolated to have only one spot in the corner. Therefore, one can assume that single-site excitation will lead to beating between several closely located corners in this $\mathcal{C}_6$-symmetric configuration (so $\mathcal{C}_3$-symmetric configuration is still advantageous for observation of such modes). One also finds that in Fig. S4(e) there are unit cells with fractional charges 1/3 and 2/3. In comparison with $\mathcal{C}_3$-symmetric configuration from the main text, there is no unit cell with fractional charge 1/2. If we remove green unit cells from the right side (or from the left side) of the purple unit cells in Fig. S4(e) (i.e. 6 green unit cells out of 12), the $\mathcal{C}_6$-symmetric configuration may be obtained with unit cells possessing 1/2, 1/3, 2/3, and 5/6 fractional charges in crystalline topological phase (the fractional charge of the orange unit cell next to the removed green unit cell changes in this case from 5/6 to 2/3, and charge for the purple unit cell changes from 2/3 to 1/2), but even in this case the cells with fractional charge 5/6 will be adjacent to each other leading to coupling of corresponding corner states.

4.2 Triangular configuration with armchair boundaries

As proposed in Refs. [1, 2], many different configurations of finite arrays with pure zigzag or armchair boundaries can be constructed. The analysis of their linear spectra shows that different fractional spectral charges indicating on the existence of topological modes with different internal structure can be encountered, in principle, also in triangular configurations with armchair edges. Linear spectrum of such an array is presented in Fig. S5(a). One can see that a variety of corner states indicated by colored lines appear in the band gap in the region, where $r/a > 1$ (the configuration is in the crystalline topological phase). The Wannier centers and distributions of spectral charges for this system at $r/a = 0.8$ and $r/a = 1.2$ are

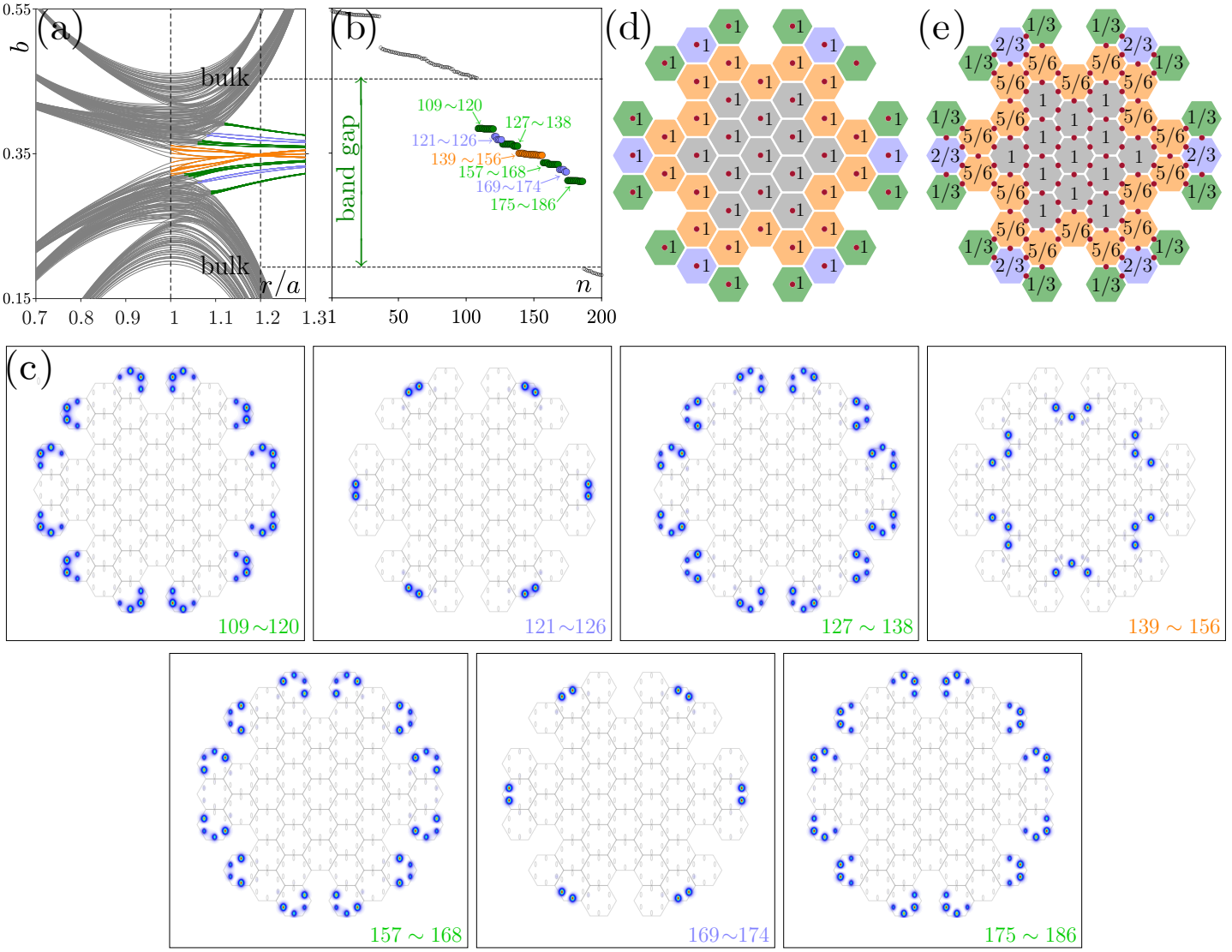

Figure S4: **Spectrum, corner states, and spectral charge of each unit cell of the $\mathcal{C}_6$ waveguide array.** (a) Linear spectrum showing dependencies of all eigenvalues versus shift parameter r at $a = 3.3$. There is a band gap between top and bottom bands of the bulk states, where various corner states appear. (b) Linear spectrum of the array at $r = 1.2a$. (c) Intensity distributions in linear corner states with different indices given in the right bottom corner of each panel. Arrangement of spectral charges at (d) $r/a < 1$ and (e) $r/a > 1$. The red dots denote the positions of the Wannier centers.

displayed in Figs. S5(d) and S5(e), respectively. In the crystalline topological phase there are unit cells with different fractional charges indicating on the possibility of formation of localized corner states in these unit cells. There are no cells with 1/3 fractional charge, but there are cells with 1/6 spectral charge in this configuration with discrete $\mathcal{C}_3$ rotational symmetry. These charges immediately find the manifestation in very different shapes of corner modes presented in Fig. S5(c). It should be mentioned that the state $n = 62$ originating from the unit cell with fractional spectral charge 5/6 that would be analogous to modes from Fig. 2(c) with numbers $112 \sim 117$ in the main text is substantially less localized in this geometry. This is because the eigenvalue of this state is very close to those of states associated with fractional charges 1/2, as indicated by the orange dots with indices $49 \sim 66$ in Fig. S5(b). The same observation can be made for state with index $n = 58$ in Fig. S5(c). One should notice that the states residing in cells with 5/6 charge in Fig. S5(e) are in fact edge states which are different from corner states numbered $112 \sim 117$ in the main text. And this is also one reason why they couple with states in the cell with 1/2 charge. As a check, one can calculate for the spectrum of a larger structure corresponding to that in Fig. S5(e), and one will find that the number of states associated with charge 5/6 will increase. In contrast, the number of states associated with spectral charge 5/6 in the main text does not change with increase of the size of

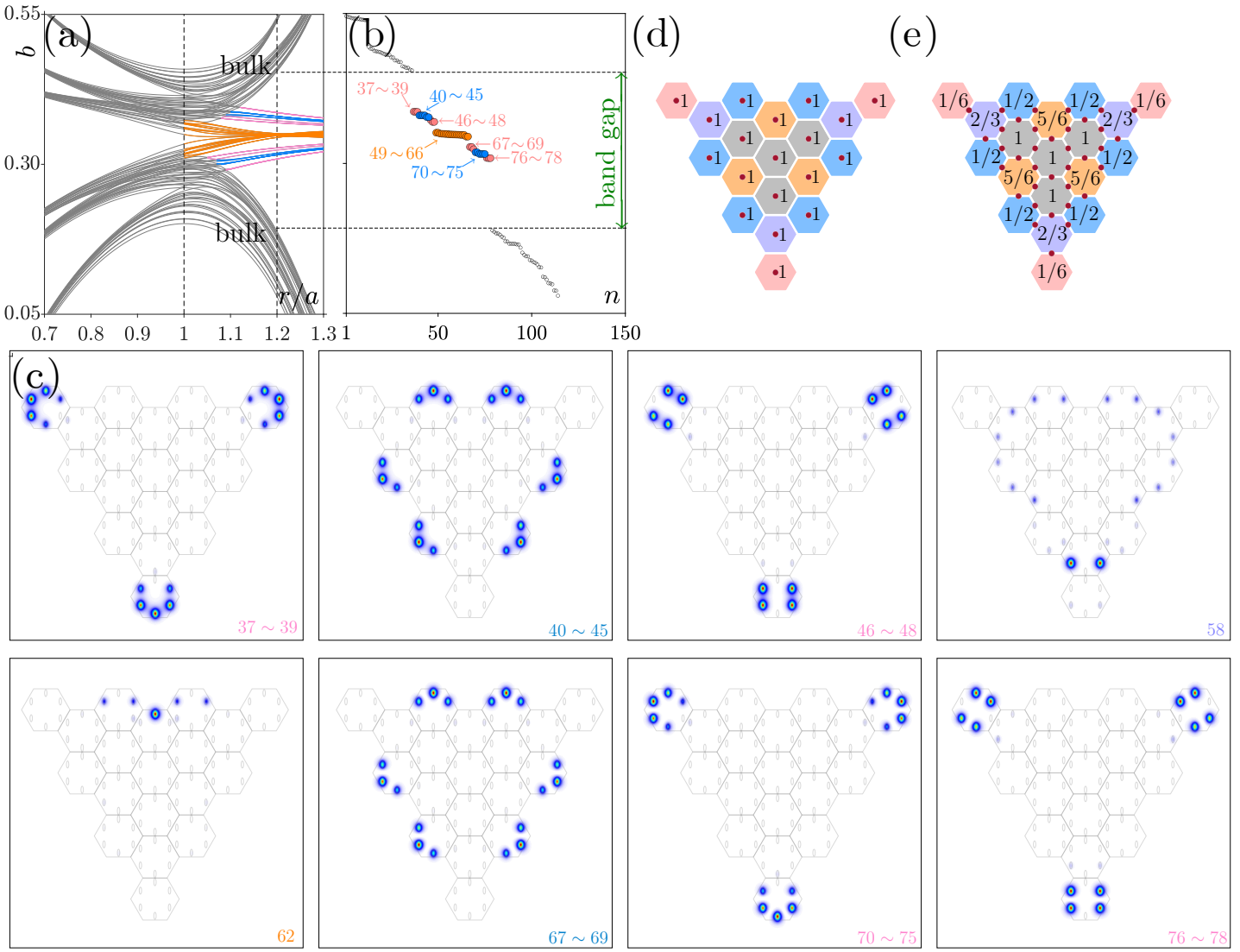

Figure S5: **Spectrum, corner states, and spectral charge of each unit cell of the triangular configuration with armchair boundaries.** (**a**) Linear spectrum showing dependencies of all eigenvalues of array modes on shift parameter r at $a = 3.3$. There is a band gap between top and bottom bands of the bulk states, where various corner states appear. (**b**) Linear spectrum of the array at $r = 1.2a$. (**c**) Intensity distributions in linear corner states with different indices given in the right bottom corner of each panel. Arrangement of spectral charges at (**d**) $r < 1.0a$ and (**e**) $r > 1.0a$. The red dots denote the position of the Wannier centers.

the structure.

4.3 The $\mathcal{H}_3$ configuration with an additional waveguide

Among the most interesting questions is what happens with corner states in the presence of strong perturbations of the underlying structure, in particular under perturbations that break discrete rotational symmetry of the structure. To answer it we study whether the corner states survive if additional site (waveguide) is added away from these states. We found that this is indeed the case, even though such operation is strong rather than weak deformation of the underlying structure. As illustrated in Fig. S6(a) in schematically shown added red "side" cell we keep only one waveguide closest to the array (its position within the red cell is also adjusted by parameter r). The spectrum of the $\mathcal{H}_3$ array with an additional side waveguide versus shift parameter r is presented in Fig. S6(b). The red line at $r/a < 1$ in the gap corresponds to a new defect mode that is strongly localized on added waveguide, while no corner states are possible in this trivial phase. Importantly, the spectrum at $r/a > 1$ in topological phase remains qualitatively the same as in original structure. By inspecting the profiles of the corner states at $r/a = 1.2$ in

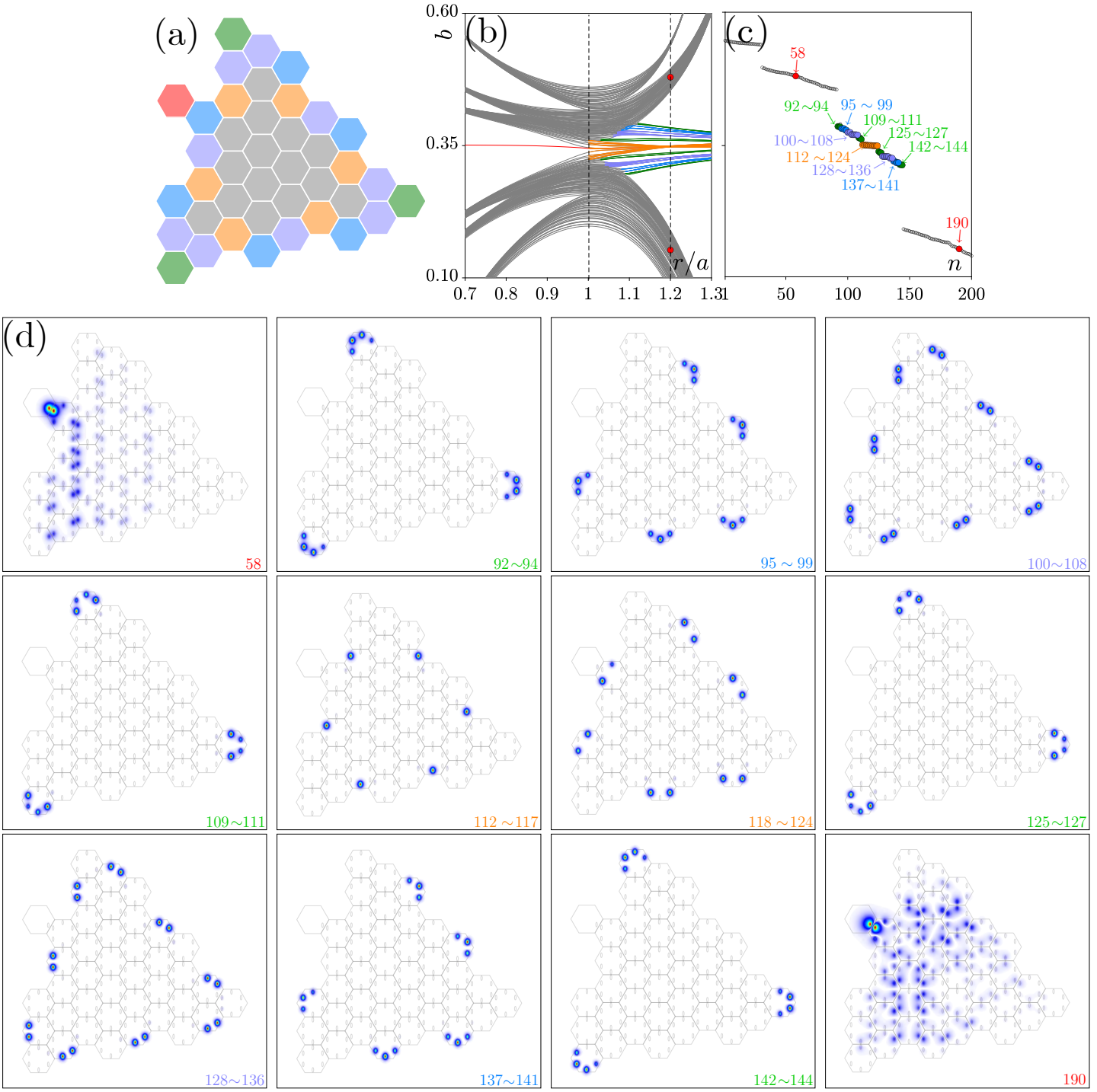

Figure S6: **Spectrum and corner states of the $\mathcal{H}_3$ array with an additional waveguide.** (a) Array configuration with the additional single waveguide in the red cell. (b) Linear spectrum showing dependencies of all eigenvalues of all modes on shift parameter r at $a = 3.3$. There is a band gap between top and bottom bands of the bulk states, where various corner states appear. (c) Linear spectrum of the array at $r = 1.2a$. (d) Intensity distributions in linear corner states with different indices given in the right bottom corner of each panel. Both states at the hybrid edge and in outer corners are shown.

Fig. S6(d), we find that the original corner states (particularly those arising due to 5/6 spectral charges) are still present in the band gap, as in Fig. 2(c) in the main text, but two new modes $n = 58$ and $n = 190$ appear that belong to bulk bands and represent delocalized states coupled to mode of newly added waveguide [see red circles in Fig. S6(c)]. Of course, because the addition of a waveguide is rather strong perturbation of the array, corner states with $n = 95 \sim 99$ and $n = 137 \sim 141$ are deformed in the very vicinity of the added waveguide (since they had maxima in the waveguide nearest to the added one). The addition of the waveguide thus "shifts" some spots from corner state into allowed band, where they couple with bulk modes [see profiles of corresponding states in Fig. S6(c) with indices 58 and 190], but corner states like $95 \sim 99$ and $137 \sim 141$ do remain in the topological gap.

5 (3+1)D simulations of excitation dynamics of nonlinear corner states

In simulations presented in the main text the temporal dynamics of sufficiently long pulses is not taken into account in 10 cm-long samples, and propagation is modeled using (2+1)D spatial nonlinear Schrödinger equation. The validity of this standard assumption for modeling of propagation dynamics in this spectral range (central wavelength of 800 nm) in fs-laser written structures can be illustrated by comparing output intensity distributions in purely spatial simulations with averaged over time intensity distributions in spatiotemporal simulations. To take into account temporal dynamics of pulses, one has to use (3+1)D Schrödinger equation accounting for both diffraction and normal dispersion of the material:

$$i\frac{\partial\psi}{\partial z} = -\frac{1}{2}\left(\frac{\partial^2}{\partial x^2} + \frac{\partial^2}{\partial y^2} - \frac{\partial^2}{\partial \tau^2}\right)\psi - \mathcal{R}(x,y)\psi - |\psi|^2\psi, \tag{S1}$$

where normalization for spatial coordinates and field amplitude ψ is the same as in main text, while time $\tau = t/t_0$ is normalized to the characteristic temporal scale $t_0 = r_0(kk'')^{1/2}$ that for our parameters ($\lambda = 800$ nm and $k'' = \partial^2 k/\partial\omega^2 \approx 36.163\,\mathrm{fs}^2/\mathrm{mm}$) is given by $t_0 \approx 6.42$ fs. Temporal FWHM of 280 fs for input pulses used in our experiments then corresponds to sufficiently large dimensionless FWHM of $T \approx 43.6$. The dispersion length for such 280 fs pulses can be evaluated as $(Tt_0)^2/4k'' \approx 0.54$ m that substantially exceeds 10 cm length of our sample. This estimate shows that dispersion should weakly affect the evolution of pulses and that temporal dynamics can in fact be disregarded. We used Eq. (S1) to model excitation of nonlinear corner state at site 2 in topological regime $r = 1.2a$ [see Fig. 6(b) from the main text]. The peak amplitude and spatial structure of the input field were the same as in main text, and we used Gaussian temporal profile providing the FWHM of $T = 43.6$. In Fig. S7 in first column we display evolution in (t, z) plane of the pulse in the center of the excited waveguide, while in second column we show output pulse profile. One can see that for first three peak power levels [corresponding to powers used in Fig. 6(b)] the pulse exhibits very weak transformations, and only for largest power level the depletion develops in the center of the pulse due to combined action of focusing nonlinearity and normal dispersion. We then compared output averaged intensity distributions in propagated 3D wavepackets at $z = 88$ corresponding to 10 cm sample length (see third column):

$$|\psi_{\mathrm{av}}(x,y)|^2 = \frac{1}{T_{\mathrm{av}}}\int_{-T_{\mathrm{av}}/2}^{T_{\mathrm{av}}/2} |\psi(x,y,t)|^2 dt,$$

where averaging interval T_{av} was selected to considerably exceed temporal width of the output pattern, with output intensity distributions $|\psi_{\mathrm{spat}}|^2$ from spatial simulations (fourth column) and found that they are practically identical. Thus, temporal dynamics indeed does not affect the conclusions about localization made in the main text and can be safely disregarded on such sample lengths.

Moreover, we repeated all experimental measurements for longer 700 fs input pulses and got similar results as for 280 fs pulses, i.e. averaged spatial intensity distributions were not affected by the increase in pulse duration. This once again confirms that temporal dynamics is not essential in this problem and can be disregarded.

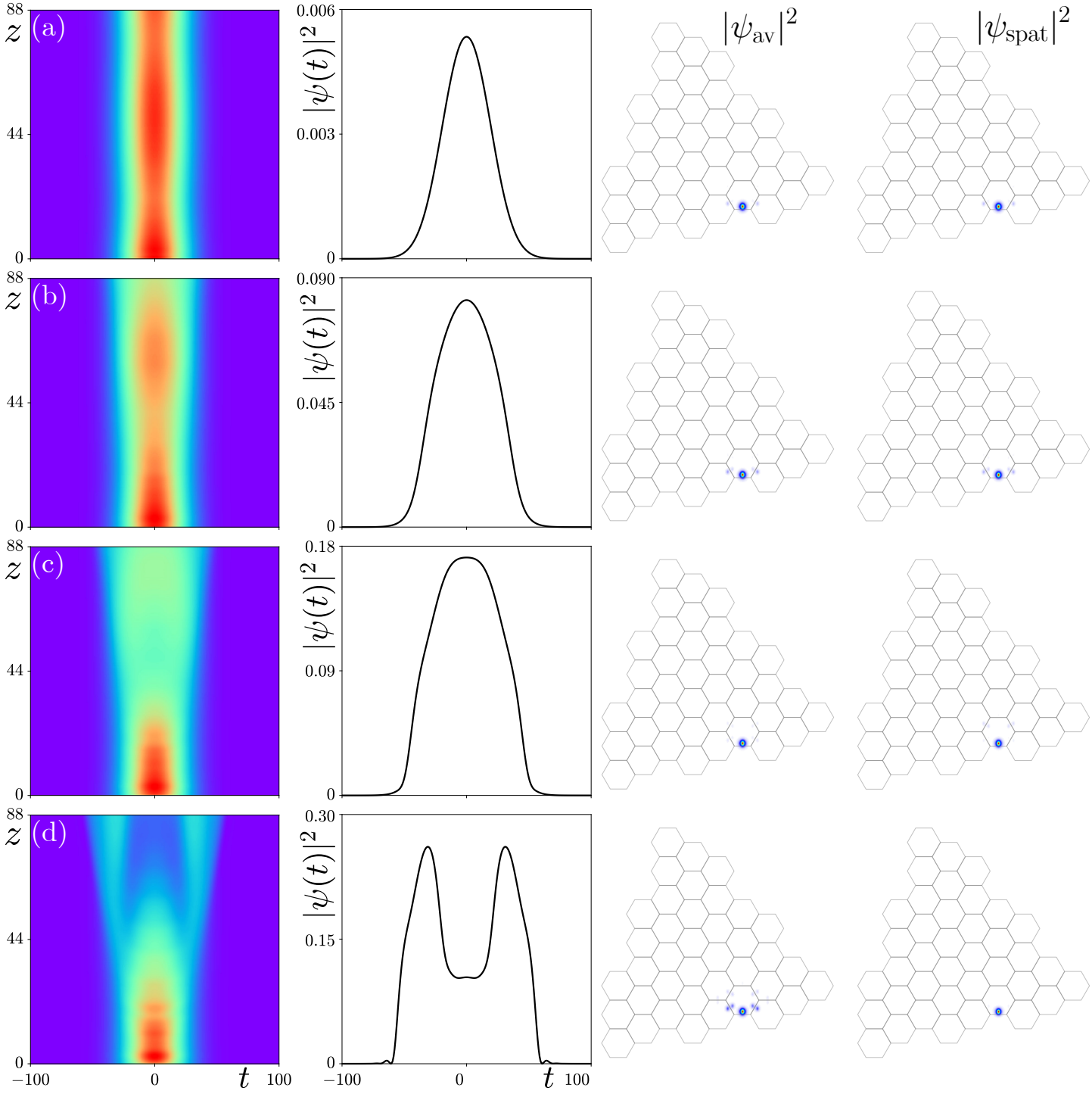

Figure S7: **Temporal dynamics of the wavepacket upon excitation of nonlinear corner states.** The figure corresponds to excitation of site 2 at $r = 1.2a$. First column shows evolution of the pulse in (t, z) plane in the excited waveguide, second column shows output temporal intensity distribution at $z = 88$ in the excited waveguide, third column shows averaged in time output intensity distributions $|\psi_{\text{av}}|^2$ from (3+1)D simulations, while fourth column shows spatial output intensity distributions $|\psi_{\text{spat}}|^2$ from (2+1)D simulations. Cases (a)-(d) correspond to power levels of $U = 0.01$, 0.20, 0.46, and 0.95 used in simulations in Fig. 6(b) in main text.

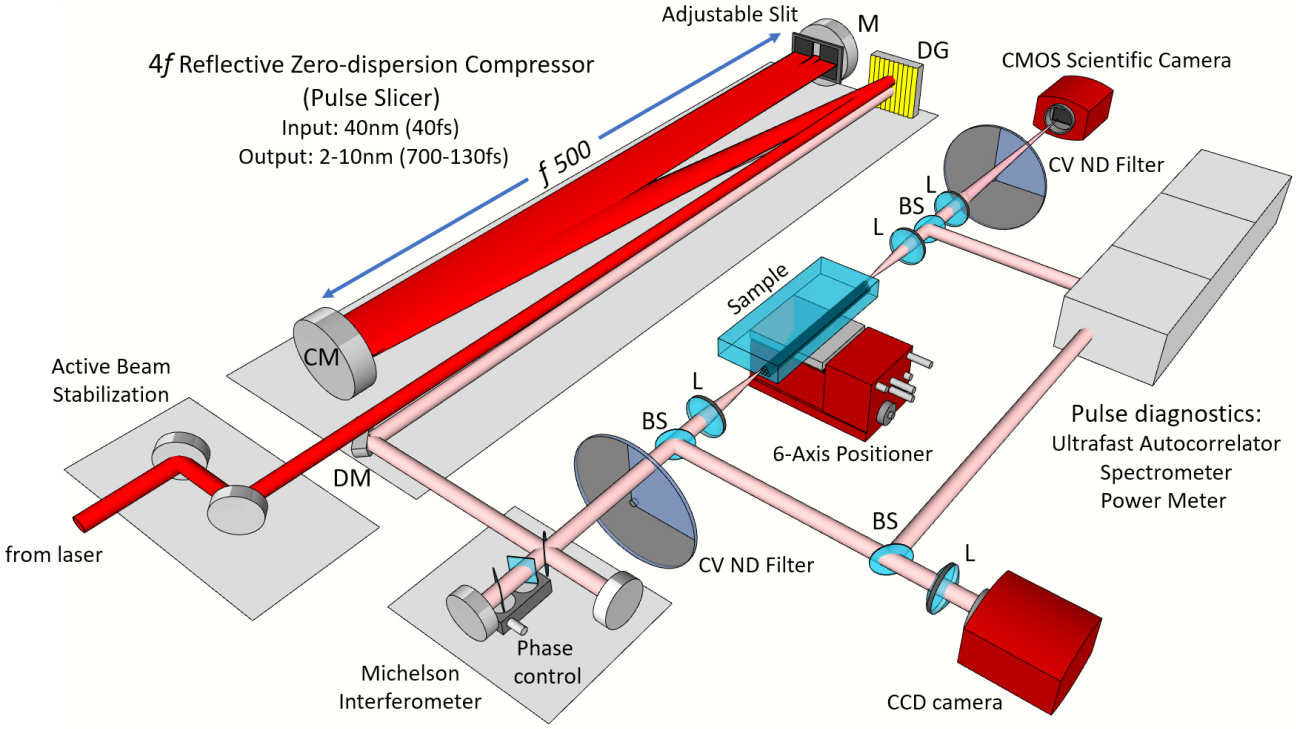

Figure S8: **Scheme of the experimental setup.**

6 Experimental setup and output spectra

The scheme of the experimental setup is displayed in Fig. S8. Initially, short pulses emitted from the 1 kHz femtosecond Ti:sapphire amplifier Spitfire HP (Spectra-Physics) with a duration of 40 fs and a broad spectrum centered at a wavelength of 800 nm arrive to the active beam stabilization system (Avesta), operating at a pulse repetition rate of 1 kHz and compensating for slow fluctuations in the spatial position of the beam. To minimize the effects due to self-phase modulation in the experiment, a $4f$ reflective zero-dispersion compressor is used. The compressor employs a $4f$ scheme, where the diffraction grating DG and flat mirror M lie in the Fourier plane of a spherical long-focus mirror CM. To adjust the spectral width and, consequently, the pulse duration, a variable slit or amplitude mask is used, allowing for a narrow spectrum ranging from 10 to 2 nm, that corresponds to a pulse duration of $130 \sim 700$ fs. The output radiation from the compressor is extracted using a D-shaped mirror (DM), positioned slightly offset in the vertical plane relative to the input beam. To enable two-waveguide excitations, a Michelson interferometer is incorporated into the setup, where phase control without spatial displacement is achieved by precise rotation of two compensation plates in one arm of the interferometer. In the case of single-waveguide excitation, one of the arms is blocked. For smooth adjustment of the input intensity, a continuously variable neutral density filter is used after the interferometer or a polarization attenuator made of a half-wave plate and a polarizer at the output of the laser system. After the interferometer, the radiation is focused into the waveguide array using an aspheric lens L with a focal length of 100 mm selected to match the waveguide mode. In order to characterize the input pulse parameters, part of the radiation is split off using an ultrafast beam splitter BS onto a CCD camera, a power meter PM100D with an S120C detector (Thorlabs), spectrometer Flame with integrating sphere FOIS-1 (Ocean Optics) and an autocorrelator PulseScout (Spectra-Physics). For precise alignment of the input radiation with the waveguide arrays, a precision 6-axis I6000 XYZ/RYP Positioner (Luminos) is used. The output distributions, attenuated by a factor of 10 using an ultrafast beam splitter BS (UFBS9010 Thorlabs), are transferred with magnification by two conjugated aspheric lenses L with focal lengths of 50 and 200 mm onto a sensitive 12.3 MP CMOS Compact Scientific Camera Kiralux (Thorlabs). To monitor the output radiation parameters, 90% of the light is reflected onto a power meter, spectrometer, or autocorrelator, as listed above. To isolate pulses from a specific waveguide in the array, a 60 μm diameter aperture is placed close to the rear face of the sample, blocking all output radiation

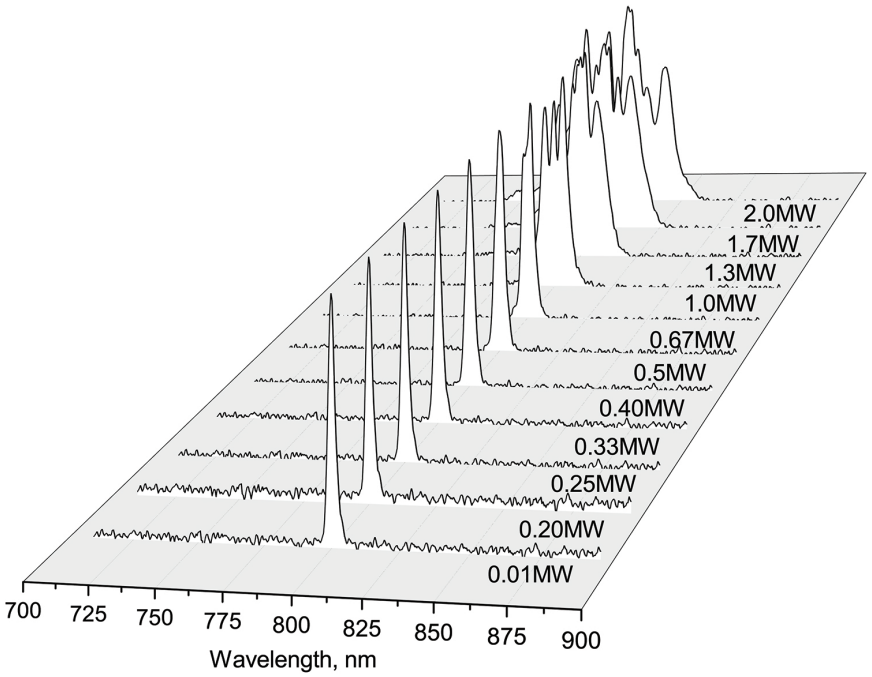

Figure S9: **Spectrum of the output pulses for excitation of site 2.** Experimentally measured output spectrum for excitation of corner site 2 versus peak power of the input pulses in the range $0.01 \sim 2.00$ MW corresponding to energies E up to 800 nJ used in experiments.

except for radiation from the waveguide under investigation.

To demonstrate that the observed corner states in topological regime with $r = 1.2a$ are indeed essentially nonlinear objects, despite the fact that for selected value of r they do not demonstrate dramatic transformations of the output intensity distributions with increase of input peak power, we additionally measured the spectra of the output pulses for the excitation of site 2 [see corresponding output intensity distributions in Fig. 6(b) in the main text]. The transformation of the output spectrum with increasing peak power is shown in Fig. S9. This power range corresponds to the pulse energies E used in the experiment (up to 800 nJ). One can observe that at peak powers above 1 MW (corresponding to 400 nJ), the pulse spectrum starts to significantly broaden due to nonlinear self-action effects. This clearly shows that corresponding corner states are nonlinear objects. This type of spectrum transformation aligns well with the results of (3+1)D numerical modeling of propagation of pulses in the same corner, discussed above.

References

[1] M. Ezawa, Peculiar width dependence of the electronic properties of carbon nanoribbons, *Phys. Rev. B* **2006**, *73* 045432.

[2] M. Ezawa, Metallic graphene nanodisks: Electronic and magnetic properties, *Phys. Rev. B* **2007**, *76* 245415.